Topological semimetal features in the multiferroic hexagonal manganites

Sophie F. Weber,[1,2] Sinéad M. Griffin,[1,2,3] and Jeffrey B. Neaton[1,2,4]
[1]*Department of Physics, University of California, Berkeley, California 94720, USA*
[2]*Molecular Foundry, Lawrence Berkeley National Laboratory, Berkeley, California 94720, USA*
[3]*Materials Science Division, Lawrence Berkeley National Laboratory, Berkeley, California 94720, USA*
[4]*Kavli Energy NanoScience Institute at Berkeley, Berkeley, California 94720, USA*

(Received 26 February 2019; revised manuscript received 7 June 2019; published 25 June 2019)

Using first-principles calculations we examine the band structures of ferromagnetic hexagonal manganites YXO_3 (X = V, Cr, Mn, Fe, and Co) in the nonpolar nonsymmorphic $P6_3/mmc$ space group. For YVO_3 and $YCrO_3$ we find a band inversion near the Fermi energy that generates a nodal ring in the $k_z = 0$ mirror plane. We perform a more detailed analysis for these compounds and predict the existence of the topological "drumhead" surface states. Finally, we briefly discuss the low-symmetry polar phases (space group $P6_3cm$) of these systems, and show they can undergo a $P6_3/mmc \rightarrow P6_3cm$ transition by condensation of soft K_3 and Γ_2^- phonons. Based on our findings, stabilizing these compounds in the hexagonal phase could offer a promising platform for studying the interplay of topology and multiferroicity, and the coexistence of real-space and reciprocal-space topological protection in the same phase.

DOI: 10.1103/PhysRevMaterials.3.064206

I. INTRODUCTION

Since their discovery in 1963 [1], the hexagonal manganites ($RMnO_3$, R = Sc, Y, In, Dy − Lu) have attracted great interest by virtue of their combined magnetic and ferroelectric order. The hexagonal manganites undergo an improper ferroelectric transition from a centrosymmetric $P6_3/mmc$ [194] phase to the polar $P6_3cm$ [185] structure ($P\bar{3}c1$ for $InMnO_3$ [2]) at around 1000 K; they develop a noncollinear antiferromagnetic ground state at much lower temperatures (for example, in $YMnO_3$, magnetic ordering sets in around 80 K [3]). Multiferroic materials such as the hexagonal manganites are interesting for both basic research and for technology due to the possibility for controlling multiple order parameters (via, for example, temperature, magnetic field, or strain) within a single material [4].

Another class of systems of current interest are topological materials, which include, more recently, topological semimetals (TSMs) [5,6]. TSMs exhibit band crossings protected by crystalline and other symmetries. The nodes in TSMs can be either zero dimensional, as in the case of Dirac and Weyl semimetals [7–13], or they can form a closed one-dimensional ring, which occurs for nodal line (NL) semimetals [14–18]. As a consequence of their nontrivial topological character, these three broad categories of TSMs host a wide variety of exotic phenomena including ultrahigh mobility, the chiral anomaly, giant magnetoresistance, and unusual surface states, such as Fermi arcs in Weyl semimetals and two-dimensional "drumhead" states in NLs [19,20].

The remarkable properties of TSMs and multiferroic materials have sparked interest in compounds that combine the two properties, i.e., multiferroic systems that are also TSMs in either their high-symmetry nonpolar or low-symmetry polar phases [21–23]. Such compounds can potentially be switched between topological and trivial electronic structure by application of an external field or by tuning temperature through the ferroelectric transition, and they also provide an excellent platform for studying the interplay between the topology, ferroelectricity, and magnetism.

There are several arguments for investigating the hexagonal manganite structure as a possible platform for combining multiferroic and TSM properties. First, the synthesis of hexagonal manganites is well developed both in bulk and in ultrathin epitaxial film form. For example, $RMnO_3$-type compounds that have an orthorhombic ground state have been grown in the metastable hexagonal structure, primarily via epitaxial stabilization on a hexagonal lattice [24]. Second, hexagonal manganites are known to exhibit real-space topological defects in their ferroelectric $P6_3cm$ state, which manifest as adjacent domains of opposite polarization directions, with the vortex phase remaining in the nonpolar $P6_3/mmc$ space group at low temperature [25]. Such nontrivial real-space topology existing concomitantly with reciprocal-space topological order, i.e., the TSM phase, would provide an unprecedented opportunity to explore the interaction between such types of topology.

While the prototypical hexagonal manganite $YMnO_3$ is insulating in both polar and nonpolar phases with its ground state antiferromagnetic (AFM) order, the band structure can be significantly altered by stabilizing ferromagnetic (FM) order. FM order can be achieved, for example, by application of a magnetic field, or by substituting other transition metal (TM) ions for Mn^{3+} to alter the balance in the competition between in-plane noncollinear AFM order and slight out-of-plane canting which has been observed in the hexagonal manganites [26].

In this work, we undertake a first-principles study of the electronic band structure and its topology in compounds isostructural to $YMnO_3$ with FM ordering. Specifically, in addition to $YMnO_3$, we investigate four other compounds in which the Mn^{3+} cation has been substituted with V^{3+}, Cr^{3+},

Fe^{3+}, and Co^{3+} in order to shift the Fermi level systematically. We predict that nonpolar hexagonal manganites YVO_3 and $YCrO_3$ have band crossings very close to the Fermi level, and in fact feature topological nodal lines in the $k_z = 0$ plane that are protected by a mirror symmetry. We also predict that they should undergo a ferroelectric (FE) $P6_3/mmc \rightarrow P6_3cm$ transition characteristic of the traditional $RMnO_3$ compounds. Stabilizing this set of compounds in the hexagonal structure should hence provide new opportunities for studying the interaction between topological and multiferroic order.

II. RESULTS

A. Methodology

For our first-principles density functional theory (DFT) calculations, we employ the Vienna *ab initio* simulation package (VASP) [27] with generalized gradient approximation (GGA) using the Perdew-Burke-Ernzerhof (PBE) functional [28] and projector augmented-wave (PAW) method [29]. We treat $4s$, $4p$, $5s$, and $4d$, and $2s$ and $2p$ electrons explicitly as valence for Y and O, respectively. For the five transition metals V-Co, we include $3p$ as well as the valence d and s electrons. To account for the localized nature of the d electrons in the transition metal cations, we add a Hubbard U correction (GGA + U) [30]. We apply the rotationally invariant version of GGA + U by Dudarev *et al.* [31], and for ease of comparison we choose a U of 3 eV for all elements, a value consistent with previous literature [32] (see Supplemental Material [33] for further discussion of our GGA + U calculations). We use an energy cutoff of 800 eV for our plane wave basis set, with a Gamma-centered **k**-point mesh of $16 \times 16 \times 6$ for the 10-atom nonpolar unit cell and $8 \times 8 \times 6$ for the 30-atom polar unit cell. Starting from the structures in the Materials Project database [34], we relax lattice parameters and internal coordinates for all structures until forces on the atoms are less than 0.001 eV/Å. We use collinear spin-polarized calculations to account for the finite magnetic moments of the transition metal (TM) ions. We do not include spin-orbit coupling (SOC) unless explicitly stated. When relevant, we approximate the noncollinear AFM order inherent to the hexagonal manganites [35] with a collinear G-type AFM ordering (GAFM), consisting of a two up, one down (one up, two down) pattern in a given 30-atom supercell for the upper (lower) basal plane [36] [see Fig. 1(b)]. Finally, for all topological analyses we use a tight-binding model constructed from our DFT-GGA + U calculations using maximally localized Wannier functions (MLWFs) [37,38] as our basis states (more details of the tight-binding model are given in the Supplemental Material [33]). For the surface state plots and surface polarization calculation we use the WannierTools software [39], which takes the tight-binding model as input. Finally, to assess dynamical stability of the YXO_3 compounds in their hexagonal form, we perform first-principles phonon calculations. The details of the computations as well as the results are described in the Supplemental Material [33].

B. Nonpolar $P6_3/mmc$ crystal structure and energetics

To begin, we focus on the centrosymmetric, nonpolar crystal structure of the hexagonal manganites in the $P6_3/mmc$ space group. This YXO_3 (X = V, Cr, Mn, Fe, and Co) structure is shown in Fig. 1(a) ($YCrO_3$ is chosen as the example). The primitive cell consists of two TM atoms, two yttrium atoms, and six oxygen atoms. The TM ions X^{3+} are fivefold coordinated by oxygen O^{2-}, forming trigonal bipyramids, and they lie in the $z = \frac{1}{4}$ and $z = \frac{3}{4}$ planes. The yttrium Y^{3+} ions are sandwiched between, in the $z = 0$ and $z = \frac{1}{2}$ planes.

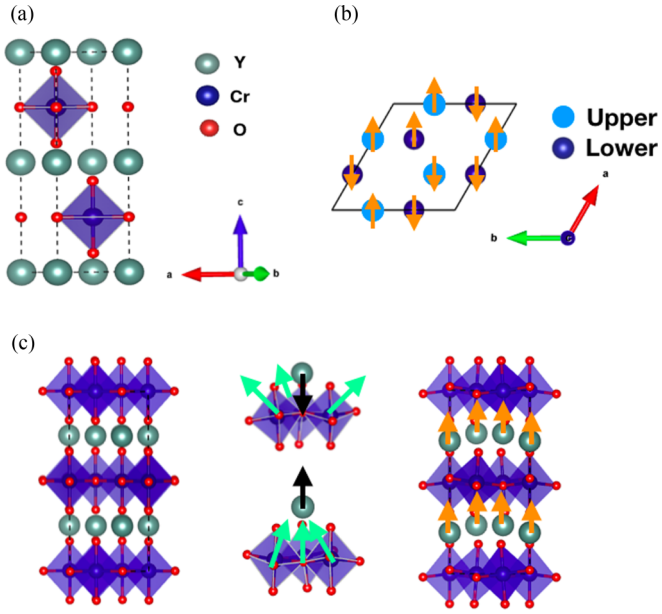

FIG. 1. (a) Primitive cell for nonpolar hexagonal $YCrO_3$, with centrosymmetric space group $P6_3/mmc$ [194]. The primitive cell consists of two Y atoms (green), two Cr atoms (blue), and six O atoms (red) (the structures of all other compounds studied in this paper are qualitatively identical). (b) Depiction of the GAFM in-plane magnetic ordering which we use as a collinear approximation to the true noncollinear antiferromagnetism in the hexagonal manganites. Note that the 10-atom $P6_3/mmc$ primitive cell is tripled to accommodate this ordering. (c) Depiction of the nonpolar-to-polar structural transition in the hexagonal manganites. Left panel: nonpolar centrosymmetric space group $P6_3/mmc$ (primitive cell tripled for easier comparison to polar phase). Middle panel: action of the unstable $q = (1/3, 1/3, 0)$ K_3 phonon on the XO_5 trigonal bipyramids. Outward trimerization pulls the Y ions downwards (top), whereas inward trimerization forces the Y ions upwards (bottom). Right panel: polar $P6_3cm$ space group. The K_3 phonon couples to a secondary order parameter, the zone-centered Γ_2^- mode (upward arrows), which further shifts the Y ions in the $\hat{z}$ direction and causes net polarization in the unit cell.

While all of our subsequent calculations are performed assuming FM order, we also perform relaxations using the GAFM configuration in order to examine the relative energies of the two magnetic states. We note that at the high temperatures for which the nonpolar $P6_3/mmc$ space group is naturally favored over the polar $P6_3cm$ space group, the structure is paramagnetic. However, it may be possible to stabilize the nonpolar structure at low temperatures, for example, by alloying or introducing defects [40]. The results of our calculations for both orderings are given in Table I. To date, the only crystal in Table I which has been synthesized in bulk $P6_3/mmc$ structure is $YMnO_3$, with reported lattice

TABLE I. Lattice constants (for the primitive 10 atom unit cell), energy per formula unit (f.u.) for FM and collinear GAFM ordering, and $\Delta E = E_{FM} - E_{GAFM}$ for YXO_3 in the $P6_3/mmc$ space group after full optimization with GGA + U. As mentioned in the main text, the inherent frustration of the GAFM ordering on a triangular lattice has a strong effect on the bond angles of YVO_3. We include the relaxed GAFM result for completeness but with the caveat that the distortion may be unphysical.

	YVO_3	$YCrO_3$	$YMnO_3$	$YFeO_3$	$YCoO_3$
FM					
a (Å)	3.496	3.510	3.617	3.566	3.640
c (Å)	12.382	12.041	11.366	11.762	11.193
E/f.u. (eV)	−42.366	−42.242	−42.188	−40.223	−37.218
GAFM					
a (Å)	3.561*	3.525	3.609	3.548	3.608
c (Å)	11.912	12.010	11.359	11.798	11.272
E/f.u. (eV)	−42.341	−42.062	−42.182	−40.407	−37.512
ΔE (eV)	−0.025	−0.180	−0.006	+0.184	+0.294

parameters $a = 3.61$ Å and $c = 11.39$ Å [41]. Comparing this to our relaxed FM GGA + U results of $a = 3.617$ Å and $c = 11.366$ Å suggests that our GGA + U calculations will be good predictors of experimental lattice constants of the other four compounds.

We also report energy differences between FM and GAFM orderings in Table I. These values may be viewed as a guide since the frustrated collinear GAFM order is an approximation to that of noncollinear AFM. Nonetheless, comparison with collinear GAFM should be useful for predicting the relative ease of stabilizing the FM state in these compounds, for example, by application of a magnetic or electric field [42]. Specifically, FM ordering becomes more stable relative to GAFM the further to the left we move on the Periodic Table, so achieving FM order should be most feasible in the V^{3+} and Cr^{3+} compounds. Note that when GAFM is enforced, for X = Cr-Co the relaxed O-X-O bond angle between apical and in-plane oxygen atoms differs by less than 0.5° from the ideal 90°. However, in the case of YVO_3 the enforced magnetic frustration results in nonuniform magnetic moments on the inequivalent V atoms, leading to a large and unrealistic distortion of the bond angles by as much as 15°. Including SOC and allowing YVO_3 to relax to the noncollinear AFM should remove this artifact, but to be consistent with the other compounds in Table I we include our results for the collinear GAFM structure; the parameters and energetics for YVO_3 with this enforced magnetic order relative to the other four compounds should be interpreted with appropriate caution.

C. Semimetal features in ferromagnetic band structures

In Fig. 2 we present the GGA + U band structures for the $P6_3/mmc$ YXO_3 compounds in the FM configuration in the absence of SOC (see the Supplemental Material [33] for GAFM band structures). Because they dominate the states near the Fermi level, we focus on the spin up bands and plot

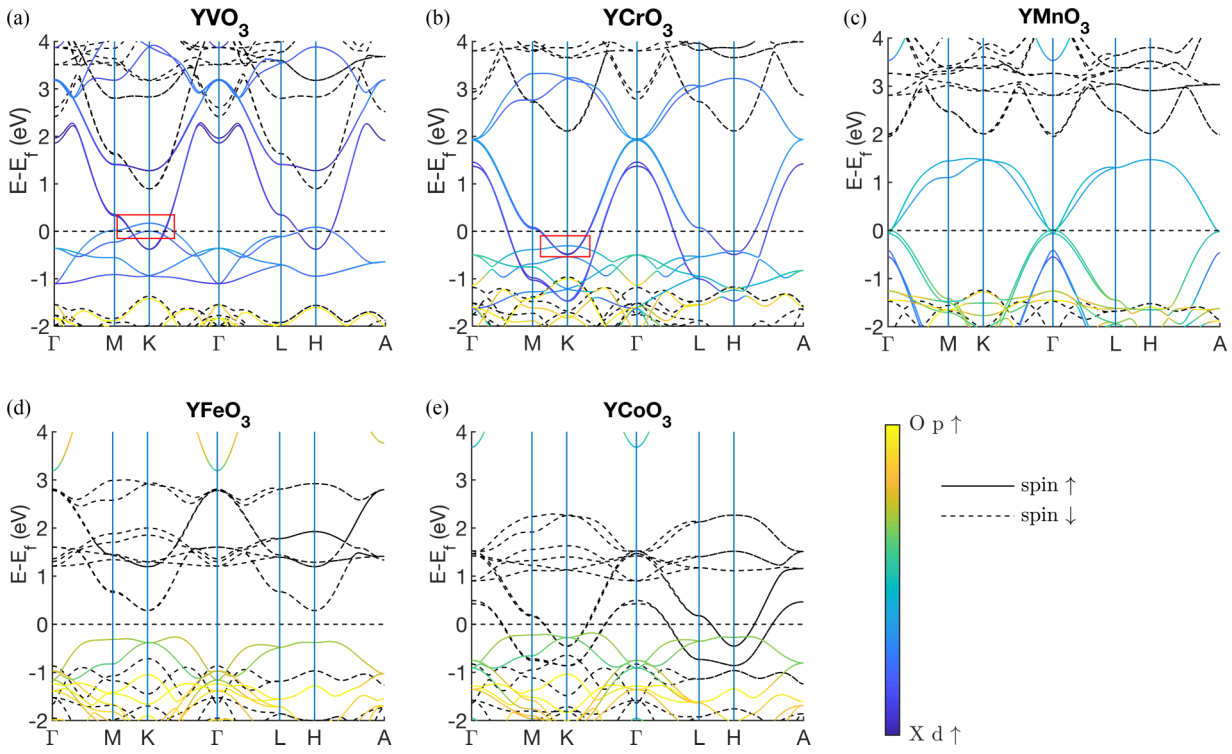

FIG. 2. Orbital-projected DFT-GGA + U ($U = 3$ eV) band structures for spin up bands in the ferromagnetic $P6_3/mmc$ YXO_3 compounds (X = V − Co), with spin down bands included without projections. The bands near the Fermi energy are composed of X d states (where X is the relevant transition metal ion) and O p states, with negligible Y character. Color scale varies from dark blue for purely X d character to yellow for purely O p character. The Fermi level is marked by the dashed black line. Panels (a)–(e) correspond to YVO_3, $YCrO_3$, $YMnO_3$, $YFeO_3$, and $YCoO_3$, respectively.

their orbital-projected character. (The spin down bands are included with dashed black lines and without orbital projection.) The spin up bands near the Fermi level are composed almost exclusively of transition metal X d states and O p states. Going from left to right across the $3d$ elements, we observe a simultaneous upwards shift of the Fermi level and a lowering in energy of the X d states toward the O p states, leading to greatest hybridization for $YFeO_3$. In YVO_3 and $YCrO_3$, the uppermost d states have started to invert energies with the lower states of mixed d and p character; in particular, for both we compute a band inversion centered at the K point $(\frac{1}{3}, \frac{1}{3}, 0)$ with linear nodes to the left and right, boxed in red (upon further inspection the apparent inversion at H is actually an anticrossing). For YVO_3, the crossings at K are about 80 meV above Fermi level, whereas for $YCrO_3$ they are about 300 meV below.

We note that GGA $+ U$ Kohn-Sham eigenvalues can only approximate single-particle excitations and band structure. Therefore, it is reasonable to question whether for GGA $+ U$, and specifically for $U = 3$ eV, our approach to computing the band structure near the Fermi energy, specifically the band inversions responsible for the nodes in YVO_3 and $YCrO_3$, will be predictive. Based on prior calculations for similar oxide systems with V and Cr in the same 3^+ oxidation state, a U of 3 eV can lead to band structures that nearly reproduce experimental gaps (see the Supplemental Material [33] for a detailed discussion). Thus we have reason to expect our $U = 3$ eV calculations will be qualitatively accurate for the band inversions near the Fermi energy.

We now further analyze the band structure and topology of YVO_3 and $YCrO_3$. Orbital decompositions of the inverted bands reveal that the conduction bands are composed of mostly V/Cr d_{xz} and d_{yz} states, whereas the valence bands are d_{xy} and $d_{x^2-y^2}$ states. Plotting only these projections, it is clear that at K the bands cross with no mixing, whereas at the $(\frac{1}{3}, \frac{1}{3}, \frac{1}{2})$ H point they hybridize, exchange character, and very slightly gap out [see Figs. 3(a) and 3(b)]. In both cases we find that the nongapped crossings in fact form nodal lines (NLs) lying in the $k_z = 0$ plane, centered at K and K' [see Fig. 3(c)].

The mirror plane symmetry $\mathcal{M}_z$ centered at $z = \frac{1}{4}$ is responsible for the protection of the NLs. (Note that with FM ordering and no SOC the magnetic space group is identical to the crystal space group $P6_3/mmc$). The action of $\mathcal{M}_z$ in reciprocal space is

$$\mathcal{M}_z : (k_x, k_y, k_z) \rightarrow (k_x, k_y, -k_z). \quad (1)$$

Thus $k_z = 0$ and $k_z = \frac{\pi}{c}$ planes are invariant under $\mathcal{M}_z$ and can be labeled by its eigenvalues, which are ± 1 in the absence of SOC. If two bands with opposite mirror eigenvalues cross on one of these planes due to a band inversion, their crossing is symmetry protected and they form a closed loop of Dirac nodes (see Supplemental Material [33] for proof that the band inversion necessarily results in a one-dimensional NL rather than discrete Dirac points). This is the case for K in the $k_z = 0$ plane. However, if the bands have the same eigenvalues they will mix and gap out [43], which occurs on the $k_z = \frac{\pi}{c}$ plane where H lies. In the Supplemental Material [33], we construct an explicit tight-binding model to calculate the $\mathcal{M}_z$ eigenvalues throughout the Brillouin zone and thus verify our observations.

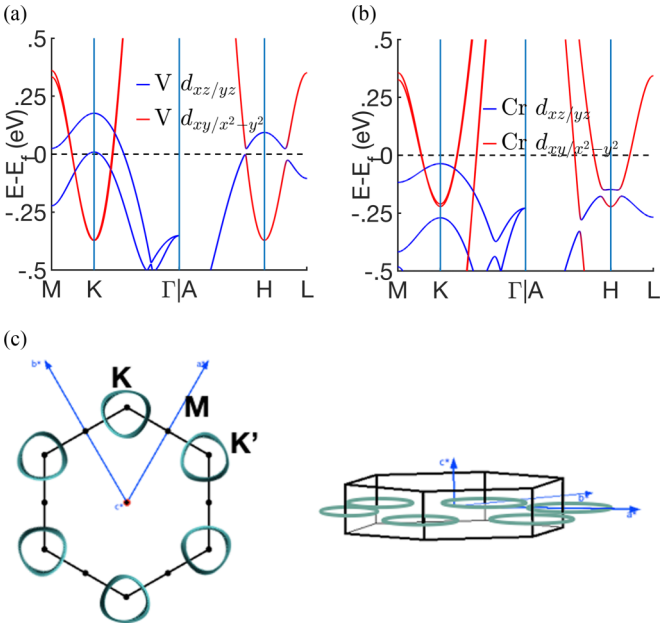

FIG. 3. Analysis of band crossings in Fig. 2. Panels (a) and (b) show zoomed-in band structures of YVO_3 and $YCrO_3$ respectively about the K and H points, with the orbital character decomposed into planar ($d_{xy}/d_{x^2-y^2}$) and z-oriented (d_{xz}/d_{yz}) d states. (c) Isoenergy contours (specifically for $E = -0.38$ eV for $YCrO_3$) in the hexagonal 3D Brillouin zone.

Let us now consider what happens when we include spin-orbit coupling (SOC). With SOC, spin and orbital degrees of freedom are coupled and symmetry operators act on both Hilbert spaces simultaneously. Notably for us, a mirror plane symmetry becomes the combination of (a) a reflection of the spatial coordinates about the mirror plane and (b) a π rotation of the spin coordinates about the axis perpendicular to the mirror plane [10]. Thus, depending on the spatial orientation of the spins, a mirror plane symmetry may either be broken or preserved when SOC is taken into account. For our nonpolar hexagonal manganites, let us first examine the case where the spin orientation is along the [001] axis. In this example, the magnetic point group symmetry is reduced from D_{6h} in the collinear case to C_{6h}. In C_{6h}, the total mirror symmetry is still preserved, since rotating the spins 180° about the z axis leaves them invariant; thus the NL should still be protected in the $k_z = 0$ plane in this case. The only difference from the non-SOC case is the functional form of $\mathcal{M}_z$ due to the requirement that the operator must now be antiunitary, such that spin up (down) bands pick up a factor of $+i$ $(-i)$ when acted on by $\mathcal{M}_z$ (we include a tight-binding model which incorporates SOC in addition to the collinear tight-binding models in our Supplemental Material [33]). Taking the example of $YCrO_3$, we plot the band structure with SOC for [001] oriented spins in Figs. 4(a) and 4(c) and as expected the crossings are still robust.

If we choose, on the other hand, to orient the spins such that they have a component perpendicular to the [001] axis, say in the [100] direction [the band structure with [100]

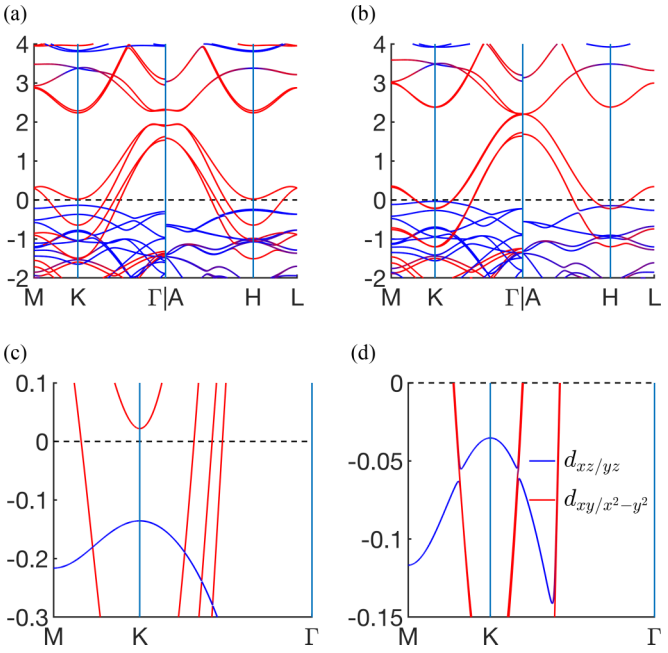

FIG. 4. DFT-GGA + U band structures with SOC, using $YCrO_3$ as the example. Planar d_{xy/x^2-y^2} character is plotted in red, while $d_{xz/yz}$ states are plotted in dark blue. Panels (a) and (b) show full band structures with SOC included and spin quantization along the [001] and [100] directions, respectively. Panels (c) and (d) show the zoomed-in portions of (a) and (b) around the K, where the topological NLs are centered in the collinear spin case. In (c) the NL crossings are still robust with the [001] spin orientation, whereas a very small gap forms between one of the conduction bands and the valence band in (d) with [100] spin orientation, with the second conduction band passing through the gap.

oriented spins is plotted in Figs. 4(b) and 4(d)], the magnetic point group is reduced to C_{2h}. Now the action of the mirror operator will still leave the orbital coordinates in the $k_z = 0$ plane unchanged, but it will send a spin with components $(s_x, s_y, s_z) = (1, 0, 0)$ to $(s_x, s_y, s_z) = (-1, 0, 0)$. Hence the mirror plane is no longer a symmetry of the crystal and generically the crossing bands can hybridize and gap out the NL. This is demonstrated in Fig. 4(d). From the orbital projection onto d_{xy/x^2-y^2} and $d_{xz/yz}$ states one can clearly see the hybridization and gap between the valence band and one of the two near-degenerate conduction bands (the second conduction band passes through the gap).

Although magnetization along any axis other than [001] will break the mirror symmetry protecting the nodal line, it is possible for discrete points along high-symmetry directions to remain ungapped. Specifically, in cases of inversion-symmetric NL systems such as YVO_3 and $YCrO_3$, if the spins are orientated along an axis $\hat{n}$ in the $a - b$ plane with a twofold rotational symmetry C_2^n, the points on the NL which intersect this axis are protected from hybridizing, and a pair of Weyl points can remain even though the rest of the NL becomes gapped [10,44]. For the point group D_{6h} there are six such axes: $C_2^{[100]}$, $C_2^{[010]}$, $C_2^{[110]}$, $C_2^{[1\bar{1}0]}$, $C_2^{[210]}$, and $C_2^{[120]}$. Thus, for the example in Figs. 4(b) and 4(d) in which the spins are oriented along [100], the $C_2^{[100]}$ rotational symmetry remains unbroken and we expect that Weyl points will remain along [100], while the rest of the line is gapped out, as seen along the $M - K - \Gamma$ path in Fig. 4(d). Unfortunately, the existence of two nearly degenerate conduction bands makes detection of the Weyl points difficult.

Finally, we note that the magnetic anisotropy energy $E_{[001]} - E_{[100]}$ is very small ([100] oriented spin is lower in energy than [001] by 1.5 meV/f.u.), implying that it should be feasible to switch between a robust and gapped nodal line within the nonpolar $P6_3/mmc$ space group by varying the direction of an external magnetic field.

D. Surface states

A hallmark feature of topological NLs is their two-dimensional "drumhead" surface states [45]. These surface states must terminate at the surface projection of the nodal line and they may lie either outside or inside the area subtended by the NL. Using our maximally localized Wannier functions (MLWFs), we construct a tight-binding slab model with 20 unit cells in the [001] direction. The 2D projected band structures on the [001] surface for YVO_3 and $YCrO_3$ are shown in Figs. 5(a) and 5(b), respectively. At the the K point, the top valence band of $YCrO_3$ and top two valence bands of YVO_3 invert with the bottom two conduction bands which are very nearly degenerate for both compounds. Thus one (two) pair(s) of NLs are actually projected onto on the [001] surface in the case of $YCrO_3$ and YVO_3, respectively, as depicted schematically in the figure insets. While in principle there is a single surface drumhead state associated with each bulk NL [15], the projected bulk from the multiple NLs interferes with the surface states, making detection difficult. However, by projecting the tight-binding wave functions onto the outermost cells in the slab we can make out a single surface state (dark blue) which has not hybridized with bulk. It is sandwiched between the pair of NLs in $YCrO_3$, whereas in YVO_3 it is visible only in the region between the two NL pairs [the corresponding regions are shaded in gray for the top-view cartoons of the [001] surface in Figs. 5(a) and 5(b)].

We can infer physical meaning from the observable surface states by calculating a series of one-dimensional Berry phases at fixed momenta $\mathbf{k}_\parallel$ parallel to the [001] surface, where the one-dimensional Berry phase θ at $\mathbf{k}_\parallel = (k_x, k_y)$ is defined by

$$\theta(\mathbf{k}_\parallel) = -i \sum_{E_n < E_F} \int_{-\pi}^{\pi} \langle u_n(\mathbf{k}) | \partial_{k_z} | u_n(\mathbf{k}) \rangle dk_z, \qquad (2)$$

where $|u_n(\mathbf{k})\rangle$ is the cell-periodic part of the Bloch eigenstate $\psi_{\mathbf{k}}(r) = e^{i\mathbf{k}\cdot\mathbf{r}} u_{n,k}(r)$ and the sum over n is over occupied states. It has been shown in previous work [46] that $\phi(\mathbf{k}_\parallel)$ is related to the bound charge on a surface perpendicular to $\mathbf{k}_\parallel$. To be more explicit, the amount of surface polarization charge $P(k_\parallel)$ (provided the band structure is gapped at $\mathbf{k}_\parallel$) is given by

$$P(k_\parallel) = \frac{e}{2\pi} \theta(\mathbf{k}_\parallel), \qquad (3)$$

modulo e, where e is the electron charge. For the case of an NL semimetal, we can divide the $\mathbf{k}_\parallel$ into distinct regions of the surface Brillouin zone, with the [001] projections of the NLs acting as region borders. For $\mathcal{M}_z$ symmetric systems

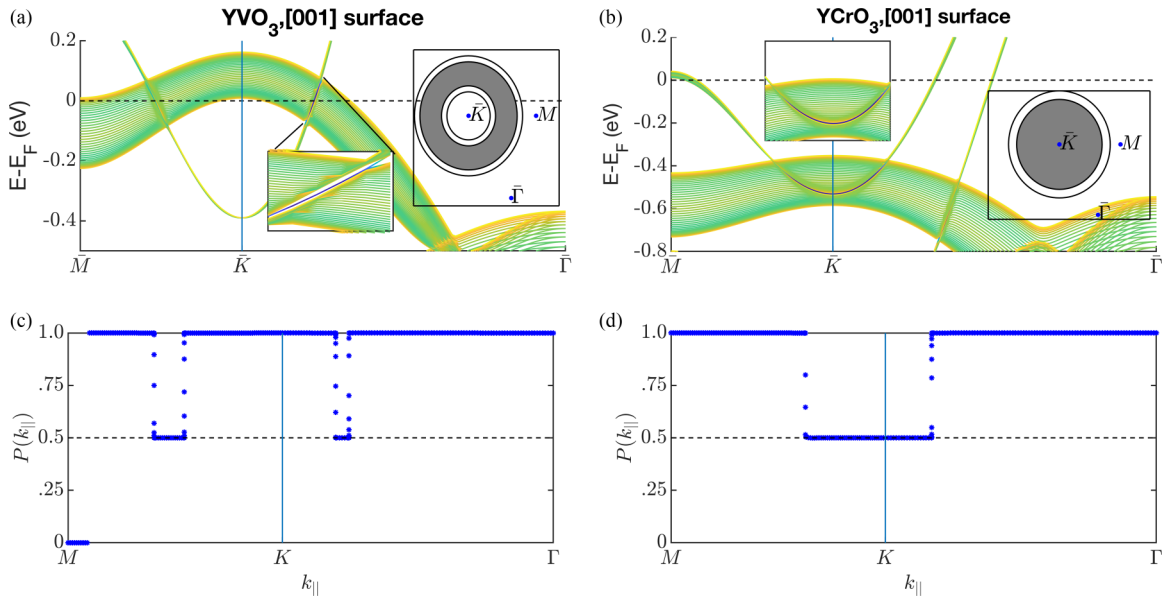

FIG. 5. Projected band structures for the [001] surface in (a) YVO_3 and (b) $YCrO_3$ from slab geometries (see text). Color is proportional to weight of projection onto the outermost layers of the slab, with blue being highest weight. The discernible surface state is magnified in one inset for both cases. The insets with the shaded circles are cartoons depicting the boundaries of the NL pairs projected onto the [001] surface, with the region where surface states appear shaded in gray. Figures (c) and (d) show the [001] surface polarization charge $P(k_\parallel)$ for YVO_3 and $YCrO_3$ respectively along the same high-symmetry path as (a) and (b). Note that $P(k_\parallel)$ jumps to a nonzero value at the same momenta where the surface states are visible.

such as YVO_3 and $YCrO_3$, $\theta(\mathbf{k}_\parallel)$ is quantized to either zero or π [and hence $P(k_\parallel)$ is quantized to zero or $\frac{1}{2}$] [45]. The NL boundaries are the only momenta at which $P(k_\parallel)$ can switch values, since all gapped $\mathbf{k}_\parallel$ within a given boundary are topologically indistinct. In fact, the $\mathbf{k}_\parallel$ at which the surface polarization charge becomes nonzero are exactly the momenta at which we expect the drumhead surface states to appear [16,45,47]. Using the hybrid Wannier charge center (WCC) method [15] we calculate $P(k_\parallel)$ for momenta in the $k_z = 0$ plane along the $M - K - \Gamma$ path for YVO_3 and $YCrO_3$ in Figs. 5(c) and 5(d), respectively. As we expect, the surface polarization is zero except at the momenta where we see the surface states, at which point it jumps to $\frac{1}{2}$.

E. Ferroelectric instabilities of the $P6_3cm$ structure

The topological NLs near the Fermi level occur in the high-symmetry $P6_3/mmc$ space group due to the combination of band inversion at K and the $\mathcal{R}_z$ mirror symmetry. However, as mentioned previously, the hexagonal manganites $RMnO_3$ are known to undergo a ferroelectric (FE) transition to the nonpolar $P6_3cm$ space group as the temperature is lowered [48]. Here we verify that the YXO_3 (X = V-Co) compounds in their metastable hexagonal structure also have a lower-energy $P6_3cm$ phase connected to the $P6_3/mmc$ topological semimetal phase through unstable phonon modes.

We first compute the energy per formula unit of the FM $P6_3cm$ polar structures and compare with our previously calculated energies for the FM $P6_3/mmc$ nonpolar structures. The GGA + U $\Delta E = E_{\text{polar}} - E_{\text{nonpolar}}$ is given in Table II. For all five compounds the polar phase is lower in energy. Next, we decompose the atomic displacements involved in the distortion from the nonpolar to the polar phase into symmetry-adapted phonon modes using the AMPLIMODES software [49,50] provided by the Bilbao Crystallographic Server. The primary structural order parameter responsible for the $P6_3/mmc \rightarrow P6_3cm$ transition in hexagonal manganites is the unit-cell tripling K_3 phonon mode at $q = (\frac{1}{3}, \frac{1}{3}, 0)$ [48,51]. As temperature is lowered this phonon can condense, leading to trimerizing tilts of the XO_5 trigonal bipyramids and a subsequent shifting either up or down of the Y ions, as shown in the middle panel of Fig. 1(c). At this point the $P6_3/mmc \rightarrow P6_3cm$ transition has already occurred, but there is no *net* polarization in the unit cell. The spontaneous polarization is caused by the coupling to K_3 of the zone-centered Γ_2^- mode at $q = (0, 0, 0)$. Γ_2^- causes an additional uniform shift of the Y ions in the $\hat{z}$ direction, resulting in nonzero polarization [52] [right panel of Fig. 1(c)]. Based on the relative amplitudes of the modes (given in Å) in the $P6_3cm$ structures relative to the parent $P6_3/mmc$ structures in Table II, we can conclude that the FE transitions in the YXO_3 compounds of interest also exhibit the K_3 mode as their primary order parameter, with the distortion caused by the Γ_2^- mode significantly smaller.

TABLE II. $\Delta E = E_{\text{polar}} - E_{\text{nonpolar}}$ and amplitudes of K_3 and Γ_2^- modes of the polar $P6_3cm$ structure with respect to $P6_3/mmc$ parent structure. Note that all calculations here are with FM ordering.

	YVO_3	$YCrO_3$	$YMnO_3$	$YFeO_3$	$YCoO_3$
ΔE (eV)	−0.354	−0.075	−0.100	−0.103	−0.358
K_3 (Å)	1.056	0.958	0.971	1.030	1.026
Γ_2^- (Å)	0.402	0.158	0.183	0.199	0.218

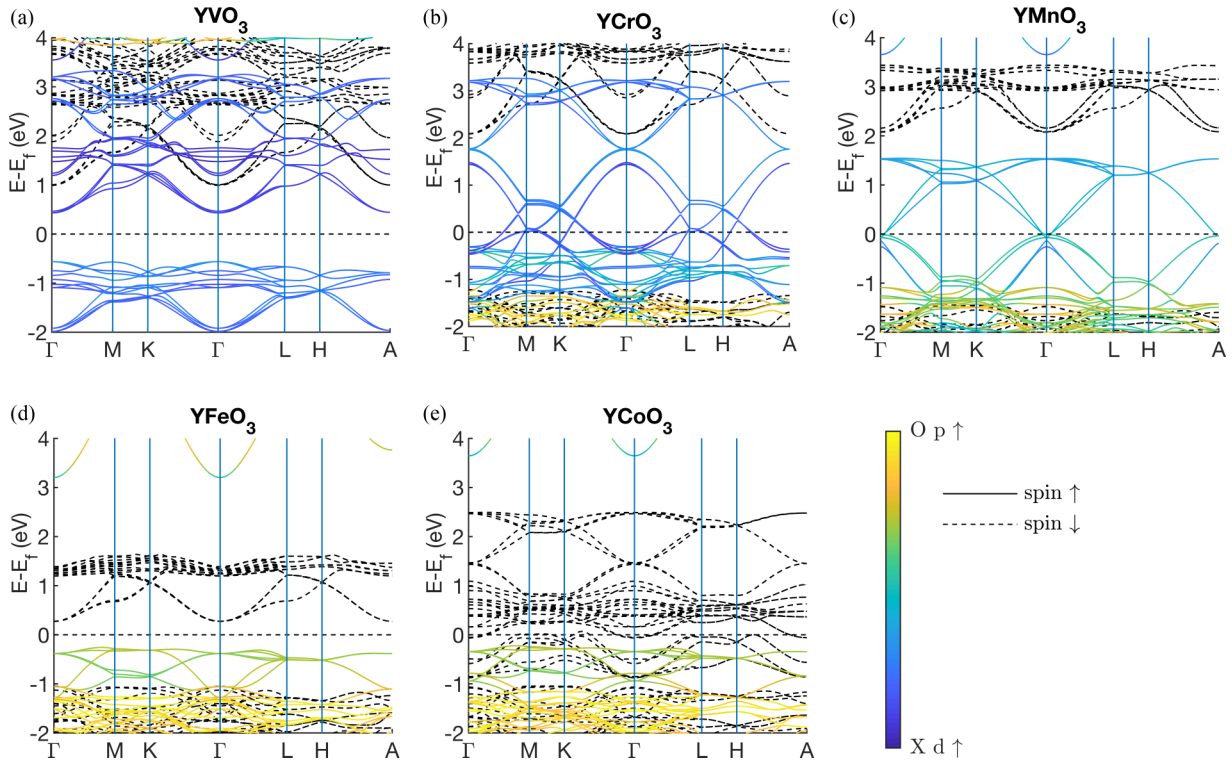

FIG. 6. DFT-GGA + U band structures for the FM YXO_3 compounds (X = V − Co) in the polar $P6_3cm$ space group. For comparison to Fig. 2, the spin-up bands are again projected onto the relevant atomic orbitals and the spin-down bands are plotted in dashed black. Panels (a)–(e) correspond to YVO_3, $YCrO_3$, $YMnO_3$, $YFeO_3$, and $YCoO_3$, respectively.

Moreover, the K_3 distortion amplitudes are all modest in magnitude, roughly 1 Å, implying that the FE transition is realistic for these systems.

Finally, we briefly examine the band structures for the fully relaxed $P6_3cm$ compounds in Fig. 6. In addition to the loss of inversion symmetry in the nonpolar-to-polar transition, the $\mathcal{R}_z$ symmetry protecting the NLs in the $P6_3/mmc$ space group is no longer a symmetry for $P6_3cm$. Thus the topological NLs in $P6_3cm$ YVO_3 and $YCrO_3$ are necessarily absent. According to our band structure calculations, $YCrO_3$ becomes a trivial metal. YVO_3, on the other hand, develops a 1 eV direct gap in Fig. 6(a). Since this would allow a tuning between a topological semimetal state and a trivial insulator by changing temperature, YVO_3 seems to be the most promising of the YXO_3 candidates for future studies.

III. CONCLUSION

In summary, we have performed extensive first-principles calculations on five YXO_3 (X = V − Co) compounds isostructural to the hexagonal manganite $YMnO_3$. We find that with FM ordering the nonpolar $P6_3/mmc$ phase hosts topologically nontrivial nodal lines near the Fermi level for YVO_3 and $YCrO_3$. The NLs are formed by a band inversion and protected by a mirror plane symmetry. We show that the YXO_3 compounds are also ferroelectric, undergoing a structural transition to polar $P6_3cm$ upon lowering of temperature. Finally, YVO_3 becomes insulating in the polar phase, suggesting the possibility of switching from a TSM to an insulating state concomitantly with the FE transition. In realizing these structures, FM magnetic order must be stabilized in the nonpolar space group; in principle, this could be done via application of a magnetic, electric, or even strain field [53]. Although all compounds except $YMnO_3$ naturally crystallize in an orthorhombic structure, rather than the hexagonal phase studied here [54–57], it is possible to synthesize a metastable structure by epitaxial growth on a hexagonal substrate. In fact, this has already been done successfully for the case of $YFeO_3$ [58]. Thus our studies provide motivation for future experimental work stabilizing the hexagonal FM phases, thereby providing a new opportunity for examining the interplay of multiferroicity and topology.

ACKNOWLEDGMENTS

This work is supported by the Center for Novel Pathways to Quantum Coherence in Materials, an Energy Frontier Research Center funded by the US Department of Energy, Director, Office of Science, Office of Basic Energy Sciences under Contract No. DE-AC02-05CH11231. Computational resources provided by the Molecular Foundry through the US Department of Energy, Office of Basic Energy Sciences, and the National Energy Research Scientific Computing Center (NERSC), under the same contract number. S.F.W. was supported under the National Defense Science and Engineering Graduate Fellowship (NDSEG). Calculations were performed on the Lawrencium cluster, operated by Lawrence Berkeley National Laboratory, and on the National Energy Research Scientific Computing Center (NERSC).

[1] E. F. Bertaut, F. Forrat, and P. H. Fang, A new class of ferroelectric: rare earth and yttrium manganites, C. R. Acad. Sci. (Paris) **256**, 1958 (1963).

[2] F.-T. Huang, X. Wang, Y. S. Oh, K. Kurushima, S. Mori, Y. Horibe, and S.-W. Cheong, Delicate balance between ferroelectricity and antiferroelectricity in hexagonal $InMnO_3$, Phys. Rev. B **87**, 184109 (2013).

[3] Z. J. Huang, Y. Cao, Y. Y. Sun, Y. Y. Xue, and C. W. Chu, Coupling between the ferroelectric and antiferromagnetic orders $YMnO_3$, Phys. Rev. B **56**, 2623 (1997).

[4] N. A. Spaldin and M. Fiebig, The renaissance of magnetoelectric multiferroics, Science **309**, 391 (2005).

[5] H. Weng, X. Dai, and Z. Fang, Topological semimetals predicted from first-principles calculations, J. Phys.: Condens. Matter **28**, 303001 (2016).

[6] S. Murakami, Phase transition between the quantum spin Hall and insulator phases in 3D: Emergence of a topological gapless phase, New J. Phys. **9**, 356 (2007).

[7] S.-Y. Xu, I. Belopolski, N. Alidoust, M. Neupane, G. Bian, C. Zhang, R. Sankar, G. Chang, Z. Yuan, C.-C. Lee, S.-M. Huang, H. Zheng, J. Ma, D. S. Sanchez, B. Wang, A. Bansil, F. Chou, P. P. Shibayev, H. Lin, S. Jia, and M. Z. Hasan, Discovery of a Weyl Fermion semimetal and topological Fermi arcs, Science **349**, 613 (2015).

[8] B. Q. Lv, H. M. Weng, B. B. Fu, X. P. Wang, H. Miao, J. Ma, P. Richard, X. C. Huang, L. X. Zhao, G. F. Chen, Z. Fang, X. Dai, T. Qian, and H. Ding, Experimental Discovery of Weyl Semimetal TaAs, Phys. Rev. X **5**, 031013 (2015).

[9] X. Wan, A. M. Turner, A. Vishwanath, and S. Y. Savrasov, Topological semimetal and Fermi-arc surface states in the electronic structure of pyrochlore iridates, Phys. Rev. B **83**, 205101 (2011).

[10] H. Weng, C. Fang, Z. Fang, B. Andrei Bernevig, and X. Dai, Weyl Semimetal Phase in Noncentrosymmetric Transition-Metal Monophosphides, Phys. Rev. X **5**, 011029 (2015).

[11] Z. K. Liu, J. Jiang, B. Zhou, Z. J. Wang, Y Zhang, H. M. Weng, D. Prabhakaran, S.-K. Mo, H. Peng, P. Dudin, T. Kim, M. Hoesch, Z. Fang, X. Dai, Z. X. Shen, D. L. Feng, Z. Hussain, and Y. L. Chen, A stable three-dimensional topological Dirac semimetal Cd_3As_2, Nat. Mater. **13**, 677 (2014).

[12] Z. K. Liu, B. Zhou, Y. Zhang, Z. J. Wang, H. M. Weng, D. Prabhakaran, S. Mo, Z. X. Shen, Z. Fang, X. Dai, Z. Hussain, and Y. L. Chen, Topological Dirac Semimetal, Na_3Bi, Science **343**, 864 (2014).

[13] Z. Wang, H. Weng, Q. Wu, X. Dai, and Z. Fang, Three-dimensional Dirac semimetal and quantum transport in Cd_3As_2, Phys. Rev. B **88**, 125427 (2013).

[14] J. Hu, Z. Tang, J. Liu, X. Liu, Y. Zhu, D. Graf, K. Myhro, S. Tran, C. N. Lau, J. Wei, and Z. Mao, Evidence of Topological Nodal-Line Fermions in ZrSiSe and ZrSiTe, Phys. Rev. Lett. **117**, 016602 (2016).

[15] G. Bian, T.-R. Chang, R. Sankar, S.-Y. Xu, H. Zheng, T. Neupert, C.-K. Chiu, S.-M. Huang, G. Chang, I. Belopolski, D. S. Sanchez, M. Neupane, N. Alidoust, C. Liu, B. Wang, C.-C. Lee, H.-T. Jeng, C. Zhang, Z. Yuan, S. Jia, A. Bansil, F. Chou, H. Lin, and M. Z. Hasan, Topological nodal-line fermions in spin-orbit metal $PbTaSe_2$, Nat. Commun. **7**, 10556 (2016).

[16] G. Bian, T.-R. Chang, H. Zheng, S. Velury, S.-Y. Xu, T. Neupert, C.-K. Chiu, S.-M. Huang, D. S. Sanchez, I. Belopolski, N. Alidoust, P.-J. Chen, G. Chang, A. Bansil, H.-T. Jeng, H. Lin, and M. Z. Hasan, Drumhead surface states and topological nodal-line fermions in $TlTaSe_2$, Phys. Rev. B **93**, 121113(R) (2016).

[17] M. Neupane, I. Belopolski, M. M. Hosen, D. S. Sanchez, R. Sankar, M. Szlawska, S.-Y. Xu, K. Dimitri, N. Dhakal, P. Maldonado, P. M. Oppeneer, D. Kaczorowski, F. Chou, M. Z. Hasan, and T. Durakiewicz, Observation of topological nodal fermion semimetal phase in ZrSiS, Phys. Rev. B **93**, 201104(R) (2016).

[18] R. Yu, H. Weng, Z. Fang, X. Dai, and X. Hu, Topological Node-Line Semimetal and Dirac Semimetal State in Antiperovskite Cu_3PdN, Phys. Rev. Lett. **115**, 036807 (2015).

[19] T. Liang, Q. Gibson, M. N. Ali, M. Liu, R. J. Cava, and N. P. Ong, Ultrahigh mobility and giant magnetoresistance in the Dirac semimetal Cd_3As_2, Nat. Mater. **14**, 280 (2014).

[20] S. A. Parameswaran, T. Grover, D. A. Abanin, D. A. Pesin, and A. Vishwanath, Probing the Chiral Anomaly with Nonlocal Transport in Three-Dimensional Topological Semimetals, Phys. Rev. X **4**, 031035 (2014).

[21] J. Tominaga, A. V. Kolobov, P. Fons, T. Nakano, and S. Murakami, Ferroelectric order control of the Dirac-semimetal phase in GeTe-Sb_2Te_3 superlattices, Adv. Mater. Interfaces **1**, 1300027 (2014).

[22] R. Li, Y. Xu, J. He, S. Ullah, J. Li, J.-M. Liu, D. Li, C. Franchini, H. Weng, and X.-Q. Chen, Weyl ferroelectric semimetal, arXiv:1610.07142v1.

[23] W. C. Yu, X. Zhou, F.-C. Chuang, S. A. Yang, H. Lin, and A. Bansil, Nonsymmorphic cubic Dirac point and crossed nodal rings across the ferroelectric phase transition in $LiOsO_3$, Phys. Rev. Materials **2**, 051201(R) (2018).

[24] I. E. Graboy, A. A. Bosak, O. Yu. Gorbenko, A. R. Kaul, C. Dubourdieu, J. P. Sénateur, V. L. Svetchnikov, and H. W. Zandbergen, HREM study of epitaxially stabilized hexagonal rare earth manganites, Chem. Mater. **15**, 2632 (2003).

[25] F.-T. Huang, X. Wang, S. M. Griffin, Y. Kumagai, O. Gindele, M.-W. Chu, Y. Horibe, N. A. Spaldin, and S.-W. Cheong, Duality of Topological Defects in Hexagonal Manganites, Phys. Rev. Lett. **113**, 267602 (2014).

[26] I. V. Solovyev, M. V. Valentyuk, and V. V. Mazurenko, Magnetic structure of hexagonal $YMnO_3$ and $LuMnO_3$ from a microscopic point of view, Phys. Rev. B **86**, 054407 (2012).

[27] G. Kresse and J. Furthmüller, Efficient iterative schemes for *ab initio* total-energy calculations using a plane-wave basis set, Phys. Rev. B **54**, 11169 (1996).

[28] J. P. Perdew, K. Burke, and M. Ernzerhof, Generalized Gradient Approximation Made Simple, Phys. Rev. Lett. **77**, 3865 (1996).

[29] P. E. Blöchl, Projector augmented-wave method, Phys. Rev. B **50**, 17953 (1994).

[30] J. P. Perdew and Y. Wang, Accurate and simple density functional for the electronic exchange energy: Generalized gradient approximation, Phys. Rev. B **33**, 8800(R) (1986).

[31] S. L. Dudarev, G. A. Botton, S. Y. Savrasov, C. J. Humphreys, and A. P. Sutton, Electron-energy-loss spectra and the structural stability of nickel oxide: An LSDA+U study, Phys. Rev. B **57**, 1505 (1998).

[32] S. Lany, Band-structure calculations for the 3d transition metal oxides in *GW*, Phys. Rev. B **87**, 085112 (2013).

[33] See Supplemental Material at http://link.aps.org/supplemental/10.1103/PhysRevMaterials.3.064206 for G-AFM nonpolar

band structures, symmetry analysis, phonon calculations, and hybrid functional calculations.

[34] A. Jain, S. P. Ong, G. Hautier, W. Chen, W. D. Richards, S. Dacek, S. Cholia, D. Gunter, D. Skinner, G. Ceder, and K. A. Persson, The materials project: A materials genome approach to accelerating materials innovation, APL Materials **1**, 011002 (2013),

[35] A. Filippetti and N. A. Hill, First principles study of structural, electronic and magnetic interplay in ferroelectromagnetic yttrium manganite, J. Magn. Magn. Mater. **236**, 176 (2001).

[36] C. G. Zhong, X. F. Jiang, H. L. Yu, Q. Jiang, J. H. Fang, and Z. Y. Li, First-principles studies of the magnetic structure and exchange interactions in the frustrated multiferroic $YMnO_3$, J. Magn. Magn. Mater. **321**, 1260 (2009).

[37] N. Marzari and D. Vanderbilt, Maximally localized generalized Wannier functions for composite energy bands, Phys. Rev. B **56**, 12847 (1997).

[38] A. A. Mostofi, J. R. Yates, G. Pizzi, Y. S. Lee, I. Souza, D. Vanderbilt, and N. Marzari, An updated version of Wannier90: A tool for obtaining maximally-localised Wannier functions, Comput. Phys. Commun. **185**, 2309 (2014).

[39] Q. S. Wu, S. N. Zhang, H.-F. Song, M. Troyer, and A. A. Soluyanov, WannierTools: An open-source software package for novel topological materials, Comput. Phys. Commun. **224**, 405 (2018).

[40] S. M. Griffin, M. Reidulff, S. M. Selbach, and N. A. Spaldin, Defect chemistry as a crystal structure design parameter: Intrinsic point defects and Ga substitution in $InMnO_3$, Chem. Mater. **29**, 2425 (2017).

[41] K. Lukaszewicz and J. Karut-Kalicinska, X-ray investigations of the crystal structure and phase transitions of $YMnO_3$, Ferroelectrics **7**, 81 (1974).

[42] T. Lottermoser, T. Lonkai, U. Amann, D. Hohlwein, J. Ihringer, and M. Fiebig, Magnetic phase control by an electric field, Nature (London) **430**, 541 (2004).

[43] C. Fang, Y. Chen, H.-Y. Kee, and L. Fu, Topological nodal line semimetals with and without spin-orbital coupling, Phys. Rev. B **92**, 081201(R) (2015).

[44] Y. J. Jin, R. Wang, Z. J. Chen, J. Z. Zhao, Y. J. Zhao, and H. Xu, Ferromagnetic Weyl semimetal phase in a tetragonal structure, Phys. Rev. B **96**, 201102(R) (2017).

[45] Y.-H. Chan, C.-K. Chiu, M. Y. Chou, and A. P. Schnyder, Ca_3P_2 and other topological semimetals with line nodes and drumhead surface states, Phys. Rev. B **93**, 205132 (2016).

[46] D. Vanderbilt and R. D. King-Smith, Electric polarization as a bulk quantity and its relation to surface charge, Phys. Rev. B **48**, 4442 (1993).

[47] M. Hirayama, R. Okugawa, T. Miyake, and S. Murakami, Topological Dirac nodal lines and surface charges in fcc alkaline earth metals, Nat. Commun. **8**, 14022 (2017).

[48] Th. Lonkai, D. G. Tomuta, U. Amann, J. Ihringer, R. W. A. Hendrikx, D. M. Többens, and J. A. Mydosh, Development of the high-temperature phase of hexagonal manganites, Phys. Rev. B **69**, 134108 (2004).

[49] D. Orobengoa, C. Capillas, M. I. Aroyo, and J. M. Perez-Mato, AMPLIMODES: Symmetry-mode analysis on the Bilbao Crystallographic Server, J. Appl. Crystallogr. **42**, 820 (2009).

[50] J. M. Perez-Mato, D. Orobengoa, and M. I. Aroyo, Acta Crystallogr., A **66**, 558 (2010).

[51] C. J. Fennie and K. M. Rabe, Ferroelectric transition in $YMnO_3$ from first principles, Phys. Rev. B **72**, 100103(R) (2005).

[52] S. M. Griffin, From the Early Universe to the Hubbard Hamiltonian in the Hexagonal Manganites, Ph.D. thesis, ETH Zurich, 2014.

[53] C. J. Fennie and K. M. Rabe, Magnetic and Electric Phase Control in Epitaxial $EuTiO_3$ from First Principles, Phys. Rev. Lett. **97**, 267602 (2006).

[54] K. Ramesha, A. Llobet, Th. Proffen, C. R. Serrao, and C. N. R. Rao, Observation of local non-centrosymmetry in weakly biferroic $YCrO_3$, J. Phys.: Condens. Matter **19**, 102202 (2007).

[55] R. Maiti, S. Basu, and D. Chakravorty, Synthesis of nanocrystalline $YFeO_3$ and its magnetic properties, J. Magn. Magn. Mater. **321**, 3274 (2010).

[56] C. R. Michel, C. C. Luhrs, and A. Cha, Synthesis of crystalline $YCoO_3$ perovskite via sol gel method, Mater. Lett. **58**, 716 (2004).

[57] A. A. Tsvetkov, F. P. Mena, P. H. M. Van Loosdrecht, D. Van Der Marel, Y. Ren, A. A. Nugroho, A. A. Menovsky, I. S. Elfimov, and G. A. Sawatzky, Structural, electronic, and magneto-optical properties of YVO_3, Phys. Rev. B **69**, 075110 (2004).

[58] S. J. Ahn, J. H. Lee, Y. K. Jeong, E. H. Na, Y. M. Koo, and H. M. Jang, Artificially imposed hexagonal ferroelectricity in canted antiferromagnetic $YFeO_3$ epitaxial thin films, Mater. Chem. Phys. **138**, 929 (2013).